JOURNAL OF SPACECRAFT AND ROCKETS
Vol. 44, No. 1, January–February 2007

Laboratory Experimentation of Autonomous Spacecraft Approach and Docking to a Collaborative Target

Marcello Romano,* David A. Friedman,† and Tracy J. Shay‡
U.S. Naval Postgraduate School, Monterey, California, 93940

DOI: 10.2514/1.22092

A new laboratory test bed is introduced that enables the hardware-in-the-loop simulation of the autonomous approach and docking of a chaser spacecraft to a target spacecraft of similar mass. The test bed consists of a chaser spacecraft and a target spacecraft simulator floating via air pads on a flat floor. The prototype docking interface mechanism of the Defense Advanced Research Projects Agency's Orbital Express mission is integrated on the spacecraft simulators. Relative navigation of the chaser spacecraft is obtained by fusing the measurements from a single-camera vision sensor and an inertial measurement unit, through Kalman filters. The target is collaborative in the sense that a pattern of three infrared light emitting diodes is mounted on it as reference for the relative navigation. Eight cold-gas on–off thrusters are used for the translation of the chaser vehicle. They are commanded using a nonlinear control algorithm based on Schmitt triggers. Furthermore, a reaction wheel is used for the vehicle rotation with a proportional derivative linear control. Experimental results are presented of both an autonomous proximity maneuver and an autonomous docking of the chaser simulator to the nonfloating target. The presented results validate the proposed estimation and control methods and demonstrate the capability of the test bed.

Nomenclature

a	=	distance of LED 1 and LED 3 from $\mathrm{CoM}_{\mathrm{tg}}$
$B(t)$, Γ_k	=	continuous-time and discrete-time input distribution matrices
b	=	distance of LED 2 from $\mathrm{CoM}_{\mathrm{tg}}$
$\boldsymbol{D}$	=	position vector from O_{nd} to the center of mass (CoM) of the chaser spacecraft (S/C)
delay(k)	=	delay of the vision sensor measurement
E	=	expected value operator
$F(t)$	=	system matrix
f	=	camera focal length
$G(t)$, Υ_k	=	continuous-time and discrete-time noise distribution matrices
H	=	measurement distribution matrix
I_{ST}	=	input signal of the Schmitt trigger
${}^{P}K_{\theta}$, ${}^{D}K_{\theta}$	=	proportional and derivative gains, respectively, of the attitude control loop
${}^{P}K_{x}$, ${}^{D}K_{x}$	=	proportional and derivative gains, respectively, of the x translation control loop
${}^{P}K_{z}$, ${}^{D}K_{z}$	=	proportional and derivative gains, respectively, of the z translation control loop
k	=	sample-time index
O_{nd}	=	nominal location, fixed to the target S/C, of the chaser CoM when chaser and target S/C are docked
O_{ST}	=	output signal of the Schmitt trigger
p_{ix}, p_{iy} $(i = 1, 2, 3)$	=	coordinates of the undistorted projections on the camera focal plane of the LEDs 1, 2, 3
$\boldsymbol{R}$	=	position vector from the CoM of the target S/C to the CoM of the chaser S/C
R_k	=	measurement noise covariance matrix at sample time k
T_y	=	torque output by the reaction wheel on the chaser spacecraft along the Y_{ch} axis
$v_{\theta\mathrm{cam}}$, $v_{x\mathrm{cam}}$, $v_{z\mathrm{cam}}$	=	noises of the vision sensor's measurement of θ, ${}^{\mathrm{tg}}x_{\mathrm{ch}}$ and ${}^{\mathrm{tg}}z_{\mathrm{ch}}$, respectively
$\boldsymbol{u}(t)$, $\boldsymbol{u}_k$	=	continuous-time and discrete-time input vectors
$\boldsymbol{v}$	=	vector of measurement noise processes
$\boldsymbol{w}(t)$, $\boldsymbol{w}_k$	=	continuous-time and discrete-time vectors of noise processes
$w_{\mathrm{acm}x}$, $w_{\mathrm{acm}z}$	=	noise of the accelerometers' measurements along X_{ch} and Z_{ch}, respectively
$w_{\beta x}$, $w_{\beta z}$	=	bias rate of the accelerometers' measurements along X_{ch} and Z_{ch}, respectively
w_{gyr}	=	noise of the gyroscope's measurement along Y_{ch}
w_{γ}	=	bias rate of the gyroscope's measurement along Y_{ch}
X_{ch}, Y_{ch}, Z_{ch}	=	chaser reference frame axes, fixed to the chaser spacecraft and with origin in its CoM
X_{tg}, Y_{tg}, Z_{tg}	=	target reference frame axes, fixed to the target spacecraft and with origin in its CoM

Received 27 January 2006; revision received 26 May 2006; accepted for publication 10 July 2006.

*Assistant Professor, Mechanical and Astronautical Engineering Department, 700 Dyer Road, Monterey, CA 93943; mromano@nps.edu. AIAA Member.
†Graduate Student, Captain U.S. Air Force.
‡Graduate Student, Lieutenant Commander U.S. Navy.

$X'_{tg}, Y'_{tg}, Z'_{tg}$ = nominal docking reference frame axes, parallel to the target reference axes and with origin in O_{nd}

${}^{ch}x_{ch}, {}^{ch}y_{ch}, {}^{ch}z_{ch}$ = components of the position vector $\boldsymbol{R}$ on the chaser reference frame

${}^{tg}x_{ch}, {}^{tg}y_{ch}, {}^{tg}z_{ch}$ = components of the position vector $\boldsymbol{R}$ on the target reference frame

${}^{tg}x'_{ch}, {}^{tg}y'_{ch}, {}^{tg}z'_{ch}$ = components of the position vector $\boldsymbol{D}$ on the nominal docking reference frame

$\boldsymbol{x}(t), \boldsymbol{x}_k$ = continuous-time and discrete-time state vector

$\tilde{\ddot{x}}_k, \tilde{\ddot{z}}_k$ = acceleration measurements output by the accelerometers along X_{ch} and Z_{ch}, respectively

$\tilde{\boldsymbol{y}}$ = measurement vector

α_0, α_1 = parameters of the Schmitt trigger

β_{xk}, β_{zk} = bias of the accelerometers' measurement along X_{ch} and Z_{ch}, respectively, at sample time k

γ_k = bias of the gyroscope's measurement along Y_{ch} at sample time k

$\Delta(\theta) = (\theta_{Ref} - \theta)$ = error between the reference and current relative attitude

$\Delta({}^{tg}x_{ch}) = ({}^{tg}x_{chRef} - {}^{tg}x_{ch})$ = error between the reference and current relative position along x

Δt = sample time

$\Delta({}^{tg}z_{ch}) = ({}^{tg}z_{chRef} - {}^{tg}z_{ch})$ = error between the reference and the current relative position along z

θ = angle from chaser reference frame to target reference frame, about Y_{tg}, positive when counterclockwise

$\hat{\theta}$ = estimate of θ output by the attitude Kalman filter

$\tilde{\dot{\theta}}_k$ = angular rate measurement output by the gyroscope along Y_{ch}

$\sigma_{gyr}, \sigma_{\gamma}$, = standard deviation of w_{gyr} and w_{γ}, respectively

$\sigma_{acmx}, \sigma_{acmz}, \sigma_{\beta x}, \sigma_{\beta z}$ = standard deviation of w_{acmx}, w_{acmz}, $w_{\beta x}$, and $w_{\beta z}$, respectively

$\sigma_{\theta cam}, \sigma_{xcam}, \sigma_{zcam}$ = standard deviation of $v_{\theta cam}$, v_{xcam}, and v_{zcam}, respectively

$\Upsilon_k Q_k \Upsilon_k^T$ = process noise covariance matrix at sample time k

Φ_k = state transition matrix at sample time k

I. Introduction

THE possibility of close monitoring, docking, refueling, and repairing satellites by using autonomous robotic vehicles will be of critical value for the design and operation of several space systems in the near future. The Hubble Space Telescope provides a clear example of possible customer spacecraft. Moreover, the autonomous proximity operation capability and the development of the associated technologies are prerequisites for the success of the envisioned sample return and human missions to the bodies of the solar system. The mishap of NASA's Demonstration of Autonomous Rendezvous Technology (DART) mission in April 2005 indicates that the mastery of autonomous spacecraft proximity operations techniques is still an open challenge.

This paragraph gives a partial historical perspective on actual space missions related to the subject of our research. Spacecraft rendezvous and docking dates back to the manned U.S. Gemini and Apollo programs and the unmanned Russian Cosmos missions of the late 1960s. In all of the American missions the astronauts were in the vehicle control loop during rendezvous and docking, while the Russians have been using an automated approach with the pilots having a supervisory role [1]. Automatic docking capability has been successfully tested by Japan during the mission ETS-VII [2]. Moreover, the European Space Agency's automated transfer vehicle is planned to leverage automatic rendezvous and docking capabilities to resupply and reboost the international space station [3]. Telerobotic maneuvering of a small inspection vehicle was tested during the 87th space shuttle mission in 1997 [4]. Autonomous on-orbit proximity navigation was tested during the Anglo-Chinese SNAP-1 mission [5] and the U.S. XSS-10 mission [6], and attempted during NASA's DART mission [7]. Finally, autonomous spacecraft docking and refueling is planned for the first in-space demonstration during DARPA's Orbital Express mission scheduled for October 2006 [8].

On-the-ground experimentation is a low-risk, relatively low-cost and potentially high-return method for validating spacecraft systems technology, navigation techniques, and control approaches, complementing analytical developments and numerical simulations. Several methods exist for hardware-in-the-loop spacecraft experimentation in a laboratory environment concerning the aspects of guidance, navigation, and control (GNC). Complete reproduction of the six degrees of freedom (DoFs) kinematics and vehicle dynamics of a spacecraft simulator moving in weightlessness can be achieved in neutral buoyancy facilities, where, nonetheless, the presence of the fluid viscosity prevents an adequate representation of the frictionless condition of the orbital flight [9]. The reproduction of the six DoFs relative motion of two spacecraft, limited only to the kinematics, can be achieved by mounting the spacecraft simulators on either cranes or robotic manipulators, as done in [10,11]. Reproduction of the three DoFs attitude kinematics and torque-free dynamics can be obtained by suspending the spacecraft simulator on a hemispherical air bearing with center of mass coinciding with the center of rotation of the bearing [12]. Finally, and this is the method used also in our research, by floating a spacecraft simulator via air pads on a flat horizontal floor it is possible to reproduce the kinematics and vehicle dynamics for three DoFs (two horizontal translations and the rotation about the vertical axis) with respected weightlessness and frictionless conditions. During the final phase of the rendezvous the in-plane and cross-track dynamics are decoupled, as modeled by the linear Hill–Clohessy–Wiltshire (HCW) equations, the reduction to three DoFs does not appear to be a critical limitation per se. It is nevertheless true that the vehicle dynamics is reduced to one of a double integrator. But, since during the final docking phase the HCW dynamics can be considered a disturbance to be compensated for by the spacecraft navigation and control system, the use of a flat floor test bed can capture many of the critical aspects of an actual autonomous docking maneuver. In particular, the interaction of the GNC algorithms with the actual dynamics of sensors, actuators, and data transmission is fully reproduced.

This paragraph reports a partial survey on planar test beds developed in support of researches on spacecraft GNC. Machida et al. [13] introduced a floating spacecraft simulator with two on-board robotic manipulators capturing a target object. The navigation and control is based on a human-in-the-loop telerobotic approach aided by a television camera, and the manipulators' motion is compensated by using inertial measurements. Ullman [14] used a conceptually similar spacecraft simulator with on-board manipulators, able to autonomously navigate on the flat floor by using data from an overhead global vision system processed by an off-board computer. An on-board vision system is used for the grasping of a free-floating object. Corazzini and How [15] used an evolution of the test bed of [14] to conduct experiments on spacecraft relative navigation by using differential global positioning system (GPS) data. Marchesi et al. [16] introduced a test bed with capabilities similar to the one of [14], but without an on-board camera. Ledebuhr et al. [17] introduced a five DoFs test bed for autonomous docking which uses stereo vision, laser distance measurements, and GPS for the navigation, and thrusters for the attitude and translation control. Nolet et al. [18] reported experiments of autonomous proximity

navigation and docking of two nanospacecraft simulators for intravehicular space applications using ultrasound sensors.

In our paper, a new three DoFs planar test bed is introduced for on-the-ground experimental validation of autonomous proximity navigation and docking maneuvers. This test bed consists of a chaser spacecraft simulator, a target spacecraft simulator, and an epoxy floating surface. The following characteristics make this test bed unique among all of the other planar test beds known to the authors:

1) The actual prototype of the docking interface mechanism of DARPA's Orbital Express mission is integrated on the chaser and target simulators and is used for the autonomous docking experiment reported in this paper.

2) The chaser spacecraft simulator is capable of independent translation control by using eight cold-gas thrusters and attitude control by using a reaction wheel. The reaction wheel allows for significant propellant conservation and extends the time endurance of single experimental runs.

3) The spacecraft simulators are completely autonomous during the experimental tests. In particular, the chaser spacecraft simulator does not require any external reference for its navigation, besides the three light emitting diodes (LEDs) mounted on the target vehicle simulator. Furthermore the vision data processing is conducted on board.

The paper describes in detail the test bed design and the navigation and control algorithms of the chaser spacecraft simulator. In particular, Kalman filtering is exploited for the relative navigation by fusing the data from the custom-developed single-camera vision sensor and the inertial measurement unit. To the knowledge of the authors, the approach used in the Kalman filters for the compensation of the vision sensor's delay is original.

The paper is organized as follows: Sec. II details the design of the experimental test bed including the floating surface, the chaser and target spacecraft simulators, and the vision sensor system. Section III introduces the methods used for the relative navigation and control of the chaser spacecraft simulator. Section IV reports the results of the experimental tests. Finally, Sec. V concludes the paper.

II. Experimental Test Bed

The autonomous docking test bed developed at the Spacecraft Robotics Laboratory of the Naval Postgraduate School consists of three main systems. These are a floating surface, a chaser spacecraft simulator, and a target spacecraft simulator (see Figs. 1 and 2). Additionally, an off-board desktop computer is used to upload software, initiate the experimental tests, and receive logged data upon their conclusion.

The main test bed systems are briefly described in the next sections. Further details are available in [19,20].

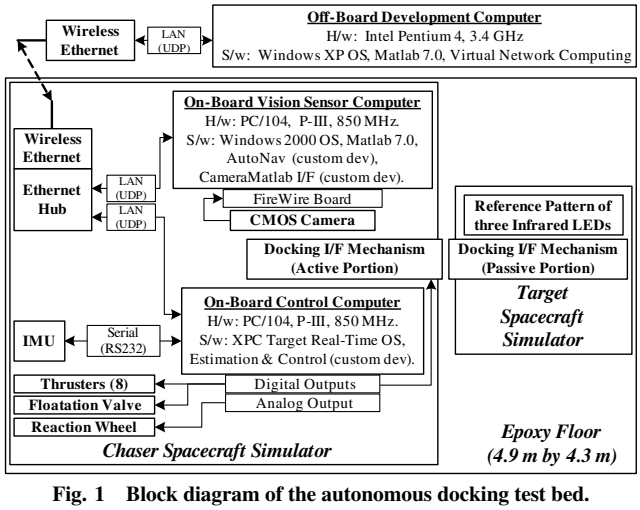

Fig. 1 Block diagram of the autonomous docking test bed.

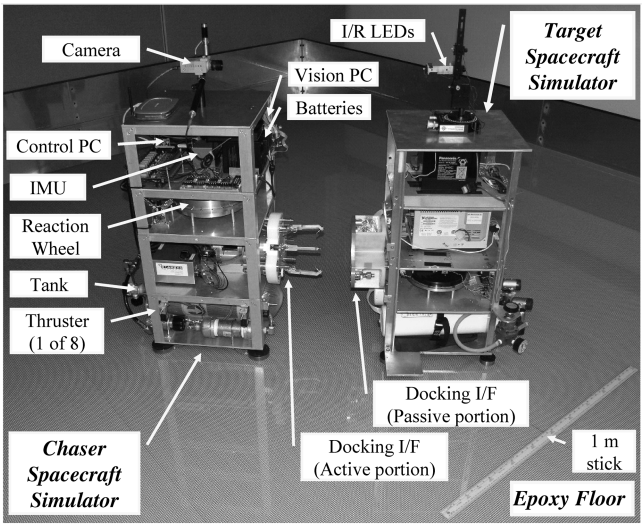

Fig. 2 Picture of the autonomous docking test bed at the Spacecraft Robotics Laboratory of the Naval Postgraduate School.

A. Floating Surface

A 4.9 m by 4.3 m wide epoxy floor surface, installed by Rock Art LTD, constitutes the base for the flotation of the chaser and target spacecraft simulators. The use of air pads on the simulators reduces the friction to a negligible level. Because of an average residual slope angle of $\sim 2.6 \times 10^{-3}$ deg for the floating surface, the average value of the residual gravity acceleration affecting the dynamics of floating vehicles is $\sim 1.4 \times 10^{-3}\ \mathrm{m \cdot s^{-2}}$. This value of acceleration, measured by analyzing the free motion of the chaser spacecraft simulation, is 2 orders of magnitude lower than the nominal amplitude of the acceleration fluctuation obtained during the reduced gravity phases of parabolic flights [21].

B. Chaser Spacecraft Simulator

The chaser spacecraft simulator consists of five modular decks mounted one on top of the other (Table 1 lists the main characteristics). This modular design allows for easy maintenance and potential upgradeability. The lowest module houses the flotation and thrust subsystems. These subsystems consist of a carbon fiber tank that feeds compressed air through two independent pressure regulators to eight thrusters and four air pads. Additionally, a surge chamber is inserted along the thrust air supply line between the regulator and the solenoid valves to limit pressure oscillations during the thrusters' operation to about $+/-2\%$ of the nominal value. Each of the eight thrusters consists of a convergent nozzle and is activated by a normally closed on–off solenoid valve. An additional solenoid valve is inserted along the flotation air supply line to allow automatic commanding of the flotation and thus avoid possible disturbances to the initial dynamic state due to manual switching.

The second deck of the simulator hosts the active portion of the docking interface mechanism. This system, designed for soft-docking applications by Starsys Research Corporation, is the prototype capture system for DARPA's Orbital Express Mission. The active portion of the mechanism consists of a motor driven lead screw that actuates three individual four-bar linkages. During the docking operation, the linkages engage the passive portion of the capture system that is mounted on the target spacecraft simulator and, by retracting, seat the passive portion into a three point kinematic mount, supported by preloaded springs, thus establishing a rigid interface. The docking interface was designed to have a relatively large envelope of possible capture misalignment. Further details on the docking interface can be found in [22].

The third and fourth decks house a reaction wheel and the electric and electronic subsystems, respectively. The reaction wheel, made by Ball Aerospace, is used for the attitude control of the vehicle. The use of a reaction wheel on the chaser vehicle provides the distinct advantage of propellant conservation and significantly extends the

Table 1 Main characteristics of the chaser spacecraft simulator

Size	Length and width	0.4 m
	Height	0.85 m
	Mass	63 Kg
	Moment of inertia about Y_{ch}	2.3 Kg m^2
Propulsion	Propellant	Air
	Equivalent storage capacity	0.72 m^3 @ 0.35 Mpa
	Operating pressure, thrust	0.35 Mpa (50 PSI)
	Operating pressure, floating	0.24 Mpa (35 PSI)
	Continuous operation	20–40 min
	Thrust of each thrusters	0.45 N
	Reaction wheel max torque	0.16 Nm
	Reaction wheel max angular momentum	20.3 Nms
Electrical & electronic subsystem	Battery type	Lithium ion
	Storage capacity	12 Ah @ 28 V
	Continuous operation	~6 h
	Computers	2 PC104 Pentium III
Sensors	IMU	Crossbow 400CC
	Vision sensor	Custom developed
	CMOS camera	Pixelink PL-A471
	Camera field of view	40 deg
	Vision Sensor Range	0–10 [m]
Docking I/F capture tolerances	Max axial misalignment	$+/-7.62$ cm
	Max lateral misalignment	$+/-5.08$ cm
	Max angular misalignment (pitch, yaw, roll)	$+/-5$ deg

time endurance of single experimental runs. At the core of the electric subsystem there are two lithium ion batteries providing 28 VDC (volts direct current) bus tension. This tension is then transformed to the other required values by an array of four DC-DC (direct current) converters. Likewise, two computers with a PC104 form factor constitute the core of the electronics subsystem. One computer is dedicated to the vision sensor (image processing and measurement data generation), while the other computer runs the real time state estimation and control code receiving data from the sensors and commanding the actuators. Additionally, the microelectromechanical-system (MEMS) based inertial measurement unit (IMU) is mounted in the center of the fourth module. The coding of the software driver for the IMU was based on [23].

Finally the fifth module houses a monochrome 1.3×10^6 pixel complementary metal oxide semiconductor (CMOS) camera and a wireless Ethernet router. The Ethernet router enables the two onboard computers to communicate with each other during the experiments and with the off-board desktop computer before and after each experiment. An infrared-pass filter is mounted on the camera lens to reject all of the objects in the field of view except the reference infrared LEDs.

C. Target Spacecraft Simulator

The target spacecraft simulator contains the passive portion of the docking interface mechanism mounted on one side. Moreover, three infrared LEDs that are used as reference for the vision sensor described below are mounted on its top deck (see Fig. 2). The target vehicle simulator was previously developed and is not actively maneuvered for the present research. Therefore, no further information on this simulator is reported here. However, additional details are available in [24].

D. Vision Sensor System

The vision sensor system is used to measure the relative position and attitude of the target spacecraft simulator with respect to the chaser spacecraft simulator. More specifically, it determines the components of the relative position vector $\boldsymbol{R}$ and the relative attitude angle θ, as depicted in Fig. 3. Without loss of generality, Fig. 3 assumes that the camera coordinates frame coincides with the chaser reference frame, centered in the chaser center of mass whereas the reference pattern frame coincides with the target frame, centered in the target center of mass.

The vision sensor consists of the following functional elements:

1) The CMOS camera is mounted on the chaser simulator and takes digital images of the target.

2) The on-board vision computer acquires the images from the camera and then processes them to determine the relative position and attitude of the target vehicle simulator using AutoNav. AutoNav is a custom-developed software program and is described later. After having performed the image processing, the vision computer transmits the data to the control computer via the on-board Ethernet network. The transmitted data consist of the relative position and angle measurements plus a check signal that is nominally 0 and becomes 1 when a new measurement is available.

3) Three infrared LEDs are mounted on board the target spacecraft simulator and serve as reference for the vision sensor system. Two LEDs are positioned along the Y_{tg} axis, while the third LED is offset and positioned along the Z_{tg} axis, as shown in Fig. 3.

The AutoNav software is the core of the vision sensor system. This software was developed in Matlab-Simulink, runs on the vision computer, and repeatedly conducts the following operations:

1) Converts the acquired image from the camera to a matrix of 8-bit-deep digital intensity values.

2) Thresholds the image by neglecting pixels with intensity value under a certain level, quantizes the image elements from 8 to 2 bits, and then transforms the full image matrix into a sparse image matrix for faster processing of the following steps.

3) Computes the centroids of the three LEDs projected onto the CMOS sensor.

4) Compensates for the radial and tangential lens assembly distortions.

5) Determines the relative position and attitude data by using the following equations based on the camera pin-hole model and the

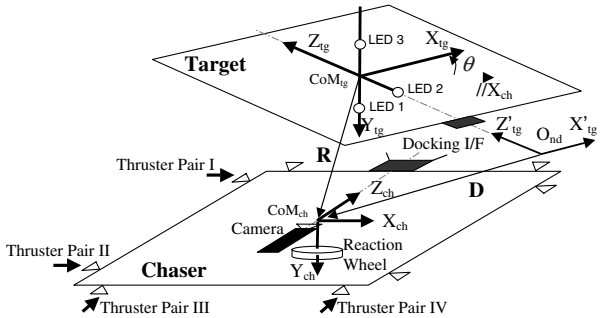

Fig. 3 Schematics of the geometry of the chaser and target spacecraft simulators floating over the epoxy flat floor.

geometry of the system:

$$
{}^{\mathrm{ch}}x_{\mathrm{ch}} = \frac{{}^{\mathrm{ch}}z_{\mathrm{ch}}p_{3x}}{f}, \qquad {}^{\mathrm{ch}}z_{\mathrm{ch}} = \frac{-2af}{\sqrt{(p_{3y}-p_{1y})^2}}
$$
$$
\theta = -\left[\eta + \frac{[{}^{\mathrm{ch}}x_{\mathrm{ch}}\cos(\eta) + {}^{\mathrm{ch}}z_{\mathrm{ch}}\sin(\eta)]}{b}\right] \tag{1}
$$

where $\eta = \arctan(p_{2x}/f)$.

By using the rotation matrix, the components of the vector $\boldsymbol{R}$ are expressed along the target reference frame, as required by the estimation algorithm described in Sec. III

$$
\begin{bmatrix} {}^{\mathrm{tg}}x_{\mathrm{ch}} \\ {}^{\mathrm{tg}}z_{\mathrm{ch}} \end{bmatrix} = \begin{bmatrix} \cos(\theta) & \sin(\theta) \\ -\sin(\theta) & \cos(\theta) \end{bmatrix} \begin{bmatrix} {}^{\mathrm{ch}}x_{\mathrm{ch}} \\ {}^{\mathrm{ch}}z_{\mathrm{ch}} \end{bmatrix} \tag{2}
$$

During the experimental tests it was advantageous to use the vector $\boldsymbol{D}$ instead of the vector $\boldsymbol{R}$ to express the relative position of the chaser with respect to the target (see Fig. 3). The components of the vector $\boldsymbol{D}$ are simply obtained by subtracting the a priori known nominal docking position from the components of $\boldsymbol{R}$ given in Eq. (2).

The camera sensor calibration, thatis, the determination of the intrinsic parameters of the camera (the focal length, the retina optical center, and the radial and tangential distortion coefficients) was a critical step in order to obtain accurate measurements with the vision sensor. Off-line calibration of the camera was conducted as described in [24].

The resulting accuracy of the developed vision sensor in the determination of the components of the relative position chaser target is $\sim$1 mm. The accuracy in the determination of the relative attitude of the chaser vehicle with respect to the target vehicle is $\sim$0.1 deg. The sample rate of the overall vision sensor system is $\sim$5 Hz, including image acquisition, image processing, and AutoNav software computation

Further details on the vision sensor system are reported in [24].

III. Navigation and Control of the Chaser Spacecraft Simulator

In the current research, we assume that the target spacecraft is attitude stabilized and that it follows a Keplerian orbit. Moreover, we consider the proximity navigation and docking maneuvers to be fast with respect to the orbital period. Therefore, we assume the target body frame to be inertial for the development of the estimation algorithm and the target spacecraft simulator to be neither rotating nor translating for the execution of our experiments.

A. Navigation Fusing Vision and Inertial Measurements

The vision sensor system described in Sec. II measures with good accuracy the relative orientation and position of the target vehicle with respect to the chaser vehicle. Nevertheless, these measurements are available asynchronously with a nominal frequency of about 5 Hz, and they are affected by a time-varying delay due to the image processing and data transmission via the onboard network. To compensate for these limitations, both the measurements of the onboard IMU and vision sensor data are exploited to assist in the state estimation of the chaser vehicle. In particular, one rate gyro measures the angle rate $\dot{\theta}$ about the Y_{ch} axis (see Fig. 3), while two accelerometers measure the components of the inertial acceleration along X_{ch} and Z_{ch}.

However, the gyro and accelerometers data are affected by noise and drift rates. Therefore, Kalman filters are employed to fuse the data from the vision sensor and the IMU. In particular, two discrete-time linear Kalman filters were implemented. The first one deals with the single DoF attitude motion while the second one deals with the two DoF translational motion. For both filters, by starting from the continuous dynamic system model

$$
\dot{\boldsymbol{x}}(t) = F(t)\boldsymbol{x}(t) + B(t)\boldsymbol{u}(t) + G(t)\boldsymbol{w}(t) \tag{3}
$$

the discrete system model can be written as

$$
\boldsymbol{x}_{k+1} = \Phi_k\boldsymbol{x}_k + \Gamma_k\boldsymbol{u}_k + \Upsilon_k\boldsymbol{w}_k \tag{4}
$$

where the noise processes, elements of $\boldsymbol{w}_k$, are assumed to be zero mean Gaussian and white, and $\Phi_k = e^{F(t_k)\Delta t}$. In particular, the process noise covariance matrix used in the propagation of the estimation error covariance is given by [25]

$$
\Upsilon_k Q_k \Upsilon_k^T = \int_{t_k}^{t_{k+1}} \int_{t_k}^{t_{k+1}} \Phi(t_{k+1},\tau)G(\tau)E[\boldsymbol{w}(\tau)\boldsymbol{w}^T(\alpha)]G^T(\alpha)\Phi^T(t_{k+1},\alpha)\,\mathrm{d}\tau\,\mathrm{d}\alpha \tag{5}
$$

The gyro and accelerometer signals are treated as inputs to the two Kalman filters with the output being an estimation of the attitude angle, the linear position and velocity, and the random biases affecting the gyro and accelerometers. The system model used in the Kalman filters is based on the kinematics of both the one-DoF attitude motion and the two-DoF translational motion experienced by the spacecraft simulator floating over the flat floor of the test bed. The measurements of the relative attitude and position from the vision sensor are used to sequentially update the state estimation whenever new data are available. The measurement equation can be written for this case as

$$
\tilde{\boldsymbol{y}}_{[k-\mathrm{delay}(k)]} = H_{[k-\mathrm{delay}(k)]}\boldsymbol{x}_{[k-\mathrm{delay}(k)]} + \boldsymbol{v}_{[k-\mathrm{delay}(k)]} \tag{6}
$$

where the elements of $\boldsymbol{v}$ are zero mean Gaussian white-noise processes. In general, the vision sensor outputs the measurements with a delay that is different for different sample times. To compensate for this delay, a measurement update is referred back to the $[k-\mathrm{delay}(k)]$th sample time, and then the state is propagated from the $[k-\mathrm{delay}(k)]$th sample time to the kth sample time using the Kalman filter propagation equations. This propagation is performed within a single sample time [i.e., between $(k-1)$ and k] using buffered values of the inputs, the state, and the state covariance matrix. The quantity $\mathrm{delay}(k)$ is evaluated by recording the time interval between the previous measurement and the current outputs of the vision sensor.

The following sections detail the two implemented Kalman filters with the standard Kalman filter update and propagation equations being used for both filters, as reported, for example, in [26].

1. Attitude Kalman Filter

The following quantities are substituted in Eq. (4) to obtain the discrete dynamic model for the attitude Kalman filter

$$
\boldsymbol{x}_k = [\theta_k\ \gamma_k]^T, \qquad \boldsymbol{u}_k = \tilde{\dot{\theta}}_k, \qquad \Upsilon_k\boldsymbol{w}_k = [w_{\mathrm{gyr}\,k}\ w_{\gamma k}]^T
$$
$$
\Phi_k = \begin{bmatrix} 1 & -\Delta t \\ 0 & 1 \end{bmatrix}, \qquad \Gamma_k = \begin{bmatrix} \Delta t \\ 0 \end{bmatrix} \tag{7}
$$

This discrete model is obtained from the continuous model in Eq. (3), with

$$
F = \begin{bmatrix} 0 & -1 \\ 0 & 0 \end{bmatrix}, \qquad B = \begin{bmatrix} 1 \\ 0 \end{bmatrix}, \qquad G = \begin{bmatrix} -1 & 0 \\ 0 & 1 \end{bmatrix} \tag{8}
$$

The following quantities are substituted in Eq. (6) to get the measurement equation of the attitude Kalman filter

$$
H_{[k-\mathrm{delay}(k)]} = [1\ 0], \qquad \boldsymbol{v}_{[k-\mathrm{delay}(k)]} = [v_{\theta\,\mathrm{cam}[k-\mathrm{delay}(k)]}] \tag{9}
$$

Finally, the process and measurement noise covariances for the attitude Kalman filter are, respectively,

$$
\Upsilon_k Q_k \Upsilon_k^T = \begin{bmatrix} \sigma_{\mathrm{gyr}}^2\Delta t + \frac{1}{3}\sigma_\gamma^2\Delta t^3 & -\frac{1}{2}\sigma_\gamma^2\Delta t^2 \\ -\frac{1}{2}\sigma_\gamma^2\Delta t^2 & \sigma_\gamma^2\Delta t \end{bmatrix}, \qquad R_k = \sigma_{\theta\,\mathrm{cam}}^2 \tag{10}
$$

2. Translation Kalman Filter

The following vectors are used for the discrete model of the translation Kalman filter, as in Eq. (4):

$$\boldsymbol{x}_k = [{}^{\text{tg}}x_{\text{ch}\,k}\ {}^{\text{tg}}\dot{x}_{\text{ch}\,k}\ \beta_{xk}\ {}^{\text{tg}}z_{\text{ch}\,k}\ {}^{\text{tg}}\dot{z}_{\text{ch}\,k}\ \beta_{zk}]^T \tag{11}$$

$$\boldsymbol{u}_k = [\tilde{\ddot{x}}_k\ \tilde{\ddot{z}}_k]^T, \qquad \Upsilon_k \boldsymbol{w}_k = [w_{\text{acm}\,xk}\ w_{\beta xk}\ w_{\text{acm}\,zk}\ w_{\beta zk}]^T \tag{12}$$

The state transition matrix and input distribution matrix for the translation Kalman filter are

$$\Phi_k = \begin{bmatrix} 1 & \Delta t & -0.5\Delta t^2\cos(\hat{\theta}_k) & 0 & 0 & -0.5\Delta t^2\sin(\hat{\theta}_k) \\ 0 & 1 & -\Delta t\cos(\hat{\theta}_k) & 0 & 0 & -\Delta t\sin(\hat{\theta}_k) \\ 0 & 0 & 1 & 0 & 0 & 0 \\ 0 & 0 & 0.5\Delta t^2\sin(\hat{\theta}_k) & 1 & \Delta t & -0.5\Delta t^2\cos(\hat{\theta}_k) \\ 0 & 0 & \Delta t\sin(\hat{\theta}_k) & 0 & 1 & -\Delta t\cos(\hat{\theta}_k) \\ 0 & 0 & 0 & 0 & 0 & 1 \end{bmatrix}, \qquad \Gamma_k = \Delta t \begin{bmatrix} 0 & 0 \\ \cos(\hat{\theta}_k) & \sin(\hat{\theta}_k) \\ 0 & 0 \\ 0 & 0 \\ -\sin(\hat{\theta}_k) & \cos(\hat{\theta}_k) \\ 0 & 0 \end{bmatrix} \tag{13}$$

where the trigonometric functions result from the use of the direction cosine matrix to transfer the accelerometers' measurements and biases from the chaser reference frame to the target reference frame.

This discrete model is obtained from the continuous model in Eq. (3), with

$$F(t) = \begin{bmatrix} 0 & 1 & 0 & 0 & 0 & 0 \\ 0 & 0 & -\cos(\theta) & 0 & 0 & -\sin(\theta) \\ 0 & 0 & 0 & 0 & 0 & 0 \\ 0 & 0 & 0 & 0 & 1 & 0 \\ 0 & 0 & \sin(\theta) & 0 & 0 & -\cos(\theta) \\ 0 & 0 & 0 & 0 & 0 & 0 \end{bmatrix}, \qquad B(t) = \begin{bmatrix} 0 & 0 \\ \cos(\theta) & \sin(\theta) \\ 0 & 0 \\ 0 & 0 \\ \sin(\theta) & -\cos(\theta) \\ 0 & 0 \end{bmatrix}, \qquad G(t) = \begin{bmatrix} 0 & 0 & 0 & 0 \\ -\cos(\theta) & 0 & -\sin(\theta) & 0 \\ 0 & 1 & 0 & 0 \\ 0 & 0 & 0 & 0 \\ \sin(\theta) & 0 & -\cos(\theta) & 0 \\ 0 & 0 & 0 & 1 \end{bmatrix} \tag{14}$$

Furthermore, the following quantities are substituted in Eq. (6) to produce the measurement equation of the translation Kalman filter:

$$H_{[k-\text{delay}(k)]} = \begin{bmatrix} 1 & 0 & 0 & 0 & 0 & 0 \\ 0 & 0 & 0 & 1 & 0 & 0 \end{bmatrix}, \qquad \boldsymbol{v}_{[k-\text{delay}(k)]} = [v_{x\,\text{cam}[k-\text{delay}(k)]}\ v_{z\,\text{cam}[k-\text{delay}(k)]}] \tag{15}$$

Finally, the process and measurement noises covariance for the translation Kalman filter are, respectively,

$$\Upsilon_k Q_k \Upsilon_k^T = \begin{bmatrix} \frac{1}{3}\sigma^2_{\text{acm}\,x}\Delta t^3 & \frac{1}{2}\sigma^2_{\text{acm}\,x}\Delta t^2 & -\frac{1}{6}\sigma^2_{\beta x}\Delta t^3\cos(\hat{\theta}_k) & 0 & 0 & -\frac{1}{6}\sigma^2_{\beta z}\Delta t^3\sin(\hat{\theta}_k) \\ \frac{1}{2}\sigma^2_{\text{acm}\,x}\Delta t^2 & \sigma^2_{\text{acm}\,x}\Delta t & -\frac{1}{2}\sigma^2_{\beta x}\Delta t^2\cos(\hat{\theta}_k) & 0 & 0 & -\frac{1}{2}\sigma^2_{\beta z}\Delta t^2\sin(\hat{\theta}_k) \\ -\frac{1}{6}\sigma^2_{\beta x}\Delta t^3\cos(\hat{\theta}_k) & -\frac{1}{2}\sigma^2_{\beta x}\Delta t^2\cos(\hat{\theta}_k) & \sigma^2_{\beta x}\Delta t & \frac{1}{6}\sigma^2_{\beta x}\Delta t^3\sin(\hat{\theta}_k) & \frac{1}{2}\sigma^2_{\beta x}\Delta t^2\sin(\hat{\theta}_k) & 0 \\ 0 & 0 & \frac{1}{6}\sigma^2_{\beta x}\Delta t^3\sin(\hat{\theta}_k) & \frac{1}{3}\sigma^2_{\text{acm}\,x}\Delta t^3 & \frac{1}{2}\sigma^2_{\text{acm}\,x}\Delta t^2 & -\frac{1}{6}\sigma^2_{\beta z}\Delta t^3\cos(\hat{\theta}_k) \\ 0 & 0 & \frac{1}{2}\sigma^2_{\beta x}\Delta t^2\sin(\hat{\theta}_k) & \frac{1}{2}\sigma^2_{\text{acm}\,x}\Delta t^2 & \sigma^2_{\text{acm}\,x}\Delta t & -\frac{1}{2}\sigma^2_{\beta z}\Delta t^2\cos(\hat{\theta}_k) \\ -\frac{1}{6}\sigma^2_{\beta z}\Delta t^3\sin(\hat{\theta}_k) & -\frac{1}{2}\sigma^2_{\beta z}\Delta t^2\sin(\hat{\theta}_k) & 0 & -\frac{1}{6}\sigma^2_{\beta z}\Delta t^3\cos(\hat{\theta}_k) & -\frac{1}{2}\sigma^2_{\beta z}\Delta t^2\cos(\hat{\theta}_k) & \sigma^2_{\beta z}\Delta t \end{bmatrix}$$

$$R_k = \begin{bmatrix} \sigma^2_{x\,\text{cam}} & 0 \\ 0 & \sigma^2_{z\,\text{cam}} \end{bmatrix} \tag{16}$$

In writing the matrix $\Upsilon_k Q_k \Upsilon_k^T$, the elements of order higher than three in Δt are neglected and it is assumed that $\sigma_{\text{acm}\,x} = \sigma_{\text{acm}\,z}$.

Table 2 lists the values of the Kalman filters' parameters used for the experimental tests reported in Sec. IV.

B. Control Using Reaction Wheel and Thrusters

The chaser spacecraft simulator employs three feedback loops to autonomously control its attitude and the two translational motion components. Figure 4 reports a block diagram representation of the control system. These feedback loops make use of the estimated relative position, velocity, attitude, and attitude rate of the target vehicle with respect to the chaser vehicle, as determined by the navigation filters introduced above.

With respect to the attitude control, the reaction wheel is commanded through the following linear proportional derivative (PD) law

$$T_y = {}^{P}K_\theta \Delta(\theta) + {}^{D}K_\theta \Delta(\dot{\theta}) \tag{17}$$

Conversely, on–off jet thrusters control the translational motion of the vehicle through the use of two nonlinear feedback control loops. These nonlinear control loops are based on the Schmitt trigger switching logic [27]. Schmitt triggers, whose output-versus-input characteristic consists of the superposition of a dead zone and a hysteresis, avoid actuators' chattering and consequent fuel waste of propellant nearby the reference state (see Fig. 5). To increase propellant saving, longer coasting phases are allowed by adding a speed-error limiter to the Schmitt triggers' switching logic.

The following linear combination of position and velocity errors of the chaser spacecraft with respect to the target spacecraft, in components along the target reference frame, are input to the Schmitt triggers

Table 2 Values of the estimation parameters

Δt	10^{-2} s
Vision sensor nominal update frequency	5 Hz
delay(k) (minimum value)	2×10^{-1} s
IMU bandwidth	133 Hz (1st order filtered at 30 Hz for antialiasing)
$\sigma_{\text{acm}\,x}$, $\sigma_{\text{acm}\,z}$	1.5×10^{-3} m $\cdot$ s$^{-3/2}$
$\sigma_{\beta x}$, $\sigma_{\beta z}$	10^{-5} m $\cdot$ s$^{-5/2}$
σ_{gyr}	1.5×10^{-3} rad $\cdot$ s$^{-1/2}$
σ_{γ}	10^{-5} rad $\cdot$ s$^{-3/2}$
$\sigma_{\theta\,\text{cam}}$	10^{-3} rad
$\sigma_{x\,\text{cam}}$, $\sigma_{z\,\text{cam}}$	10^{-3} m
P_0 (attitude filter initial covariance)	diag[10^{-15} 10^{-8}]
P_0 (translation filter initial covariance)	diag[10^{-8} 10^{-15} 10^{-8} 10^{-8} 10^{-15} 10^{-8}]
Initial state condition (attitude filter)	$[0\ \ 0]^T$
Initial state condition (translation filter)	$[0\ \ 0\ \ 0\ \ 0\ \ 0\ \ 0]^T$

$$
\begin{aligned}
I_{\text{ST}x} &= {}^{P}K_x \Delta({}^{\text{tg}}x_{\text{ch}}) + {}^{D}K_x \Delta({}^{\text{tg}}\dot{x}_{\text{ch}}) \\
I_{\text{ST}z} &= {}^{P}K_z \Delta({}^{\text{tg}}z_{\text{ch}}) + {}^{D}K_z \Delta({}^{\text{tg}}\dot{z}_{\text{ch}})
\end{aligned}
\tag{18}
$$

Limiters are applied to both the position and the speed errors to save propellant by realizing a bang-coast-bang motion.

The two Schmitt trigger blocks output the requested thrust components along the target reference frame. A thruster mapping algorithm is then used to transform these commands into requested thrust components along the chaser reference frame. This is consistent with the on-board actuators which provide thrust in directions fixed to the chaser spacecraft.

The thruster mapping block operates a coordinate transformation, normalizes the thrust commands, and outputs a set of two analog signals, with values between -1 and $+1$. The first signal corresponds to the two thruster pairs along X_{ch} (designated by indexes I and II in Fig. 3); in particular, a positive value of this signal corresponds to a requested thrust along the positive value of X_{ch} while a negative value corresponds to a requested thrust in the opposite direction. The magnitude of the signal is the value of requested thrust normalized by the maximum thrust given by two thrusters operating together. The second signal corresponds to the two thruster pairs along Z_{ch} (designated by indexes III and IV in Fig. 3) with analogous meaning of the sign and magnitude.

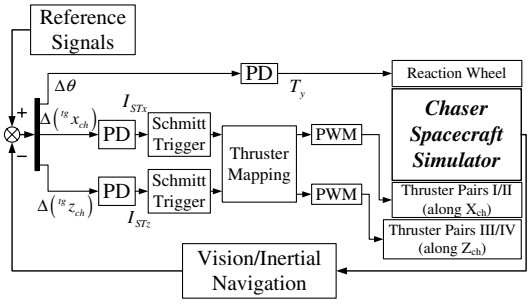

Fig. 4 Block diagram of the control system of the chaser spacecraft simulator.

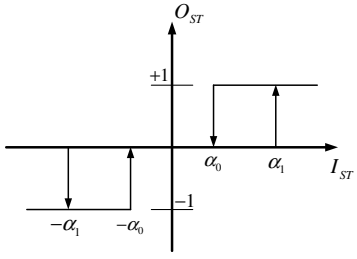

Fig. 5 Output-versus-input characteristics of the Schmitt trigger.

Table 3 Values of the control parameters

Sample time	10^{-2} s
${}^{P}K_{\theta}$	1.5
${}^{D}K_{\theta}$	2.5 s
${}^{P}K_x$	1 if $\lvert\Delta({}^{\text{tg}}x_{\text{ch}})\rvert < \max\lvert\Delta({}^{\text{tg}}x_{\text{ch}})\rvert$, 0 otherwise
${}^{P}K_z$	1 if $\lvert\Delta({}^{\text{tg}}z_{\text{ch}})\rvert < \max\lvert\Delta({}^{\text{tg}}z_{\text{ch}})\rvert$, 0 otherwise
${}^{D}K_x$	1.6 s if $\lvert\Delta({}^{\text{tg}}\dot{x}_{\text{ch}})\rvert < \max\lvert\Delta({}^{\text{tg}}\dot{x}_{\text{ch}})\rvert$, 0 otherwise
${}^{D}K_x$	1.6 s if $\lvert\Delta({}^{\text{tg}}\dot{z}_{\text{ch}})\rvert < \max\lvert\Delta({}^{\text{tg}}\dot{z}_{\text{ch}})\rvert$, 0 otherwise
α_0 (for both Schmitt triggers)	1.5×10^{2} m
α_1 (for both Schmitt triggers)	2×10^{-2} m
max $\lvert\Delta({}^{\text{tg}}x_{\text{ch}})\rvert$ and max $\lvert\Delta({}^{\text{tg}}z_{\text{ch}})\rvert$	4×10^{-2} m
max $\lvert\Delta({}^{\text{tg}}\dot{x}_{\text{ch}})$	5×10^{-3} m $\cdot$ s^{-1}
max $\lvert\Delta({}^{\text{tg}}\dot{z}_{\text{ch}})$	1.5×10^{-2} m $\cdot$ s^{-1}
PWM min pulse width	3.3×10^{-2} s
PWM sample time	4×10^{-1} s

Each of the two outputs of the thruster mapping block are fed into a separate pulse width modulation (PWM) block. Each PWM block is then used to obtain an approximately linear duty cycle from on–off actuators by modulating the opening time of the solenoid valves [28]. Finally, the digital outputs (either zero or one) of each pulse width modulator command four thrusters. That is the first PWM block commands the thrusters of pairs I and II, while the second PWM block commands the thrusters of pairs III and IV. Because the thrusters are employed only for translation and not for attitude control, the commands are the same for pairs I and II, and for pairs III and IV.

Table 3 lists the values of the control parameters used for the experimental tests reported in Sec. IV. In particular, the proportional and derivative gains of the attitude control loop were determined by imposing a damping ratio of 0.7 for the second order system defined by the moments of inertia about the axis Y_{ch}, the maximum torque output by the reaction wheel and a chosen saturation error of 4 deg. The values of the Schmitt trigger parameters were chosen to have a nominal resulting limit cycle amplitude of 1.8 cm. Furthermore, the minimum opening time of the PWM was based on the experimentally measured bandwidth of the thrusters' solenoid valves.

IV. Experimental Results

The navigation and control algorithms introduced above have been coded in Matlab-Simulink and run in real time on the onboard computer of the chaser spacecraft simulator during the experimental tests.

Two experimental tests are presented here as significant samples of autonomous maneuvers of the chaser spacecraft simulator in proximity of the target spacecraft simulator. During both experiments, the target vehicle is kept fixed. The first maneuver consists of autonomously tracking a closed path in front of the target, while the second maneuver consists of autonomously approaching the target and finally docking to it. These experimental tests validate our navigation and control approach and demonstrate the capability of the test bed system.

A. Experimental Test 1: Autonomous Proximity Maneuver Along a Closed Path

Figures 6 and 7 report the results of the first experimental test. During this test a closed path is followed by the chaser spacecraft simulator. The reference path for the center of mass of the chaser vehicle consists of 24 way points, taken at angular intervals of 15 deg along a circle of diameter of 0.6 m with center at the point

$$
{}^{\text{tg}}x'_{\text{ch}} = 0 \text{ m}; \qquad {}^{\text{tg}}z'_{\text{ch}} = -0.92 \text{ m} \tag{19}
$$

The reference attitude motion of the chaser vehicle is given by the following signal, which aims to keep the onboard camera always directed toward the target

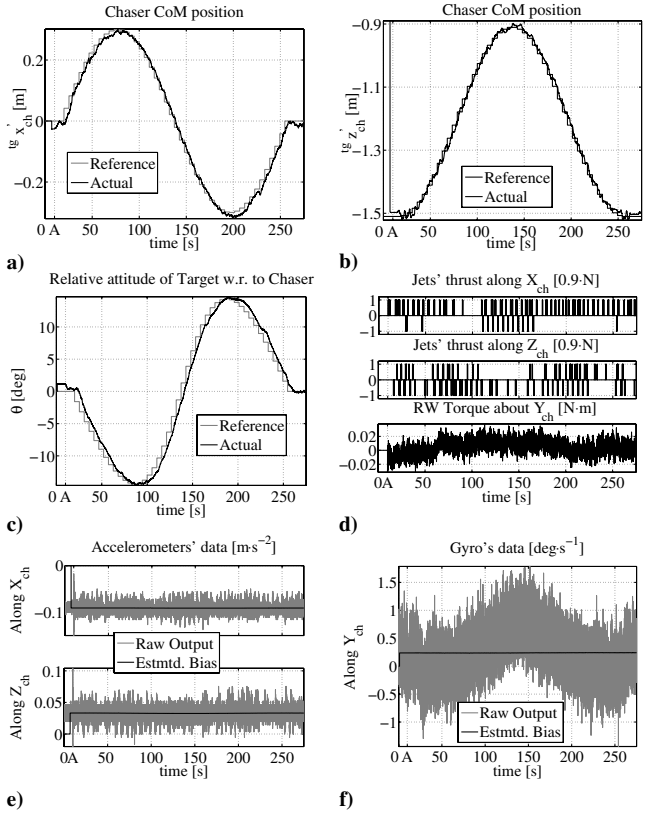

Fig. 6 Results of experimental test 1, autonomous proximity maneuver along a closed path: logged data versus time. The chaser spacecraft simulator starts to float over the epoxy floor at time $A = 10$ s. a) Tansversal position of the center of-mass of the chaser with respect to the target; b) longitudinal position of the center of mass of the chaser; c) relative attitude; d) actuators' actions; e) accelerometers' data; and f) gyroscope's data.

$$\theta_{\mathrm{Ref}}(t) = \mathrm{atan}\left[\frac{{}^{\mathrm{tg}}x_{\mathrm{ch\ Ref}}(t)}{{}^{\mathrm{tg}}z_{\mathrm{ch\ Ref}}(t)}\right] \tag{20}$$

The entire maneuver lasts 275 s. During the first 10 s, the chaser vehicle is maintained fixed whereas the Kalman filters, which are based on the measurements from the vision sensor and the IMU, converge to a solution. In particular, the attitude Kalman filter is switched on at time = 1 s and subsequently the translation Kalman filter, which needs the attitude estimated by the first filter, is switched on at time = 6 s. At 10 s into the experiment, the solenoid valve regulating the air flow to the air pads is opened and the chaser vehicle begins to float over the epoxy floor. At this point, the vehicle begins to maneuver through autonomous control of the eight thrusters and the reaction wheel.

As evidenced in Figs. 6e and 6f, the navigation Kalman filters correctly estimate the biases of the accelerometers and gyroscopes.

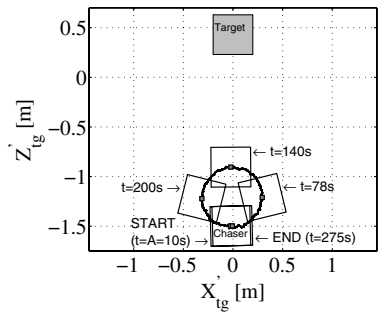

Fig. 7 Results of experimental test 1, autonomous proximity maneuver along a closed path: bird's-eye view of the motion of the chaser spacecraft simulator on the epoxy floor. The line indicates the ground track of the chaser center of mass. The empty squares are snapshot sketches of the chaser vehicle at significant time instants during the maneuver.

Figures 6a and 6b show that the components on the target reference frame of the center-of-mass position of the chaser vehicle, estimated by the translation Kalman filter, are kept close to the reference signals by the action of the thrusters during the overall maneuver. More specifically, the mean of the absolute value of the tracking error is 1.3 cm for $\Delta({}^{\mathrm{tg}}x'_{\mathrm{ch}})$, with standard deviation of 1.1 cm, and 1 cm for $\Delta({}^{\mathrm{tg}}z'_{\mathrm{ch}})$ with standard deviation of 7.5 mm. These control accuracy values are in good agreement with the set parameters for the Schmitt trigger. Finally, Fig. 6c demonstrates the accuracy of the attitude tracking control through a comparison of the reference and actual attitude motion. In this case, the mean of the absolute value of the tracking error $\Delta(\theta)$ is 0.98 deg, with standard deviation of 0.69 deg.

Figure 6d reports the command signals to the actuators. The commands to the thrusters, which are normalized to the thrust value provided by two thrusters (0.9 N), show that the Schmitt trigger control logic successfully avoids chattering behavior. The noise in the reaction wheel command is due to the use of the unbiased, but still noisy, gyroscopes' data for the estimation of $\dot{\theta}$ in the control law of Eq. (17). However, this noise is not an issue because it is filtered by the low bandwidth rotational dynamics of the chaser vehicle system. This bandwidth has a value of $\sim$0.14 Hz, as determined by considering the vehicle moment of inertia, the reaction wheel maximum torque, and the set control parameters.

Figure 7 shows a bird's-eye view of the chaser spacecraft simulator motion. Of particular note, the attitude motion aiming to maintain target pointing is clearly visible. Moreover, the good control accuracy can be qualitatively evaluated by the closeness of the ground-track line to a circle and of the initial configuration of the chaser vehicle to the final one.

The equivalent volume of propellant air consumed during this experimental test was $\sim$0.1 m^3 (at the reference pressure of 0.35 MPa that corresponds to the thruster's operating value).

B. Experimental Test 2: Autonomous Approach and Docking to the Target

Figures 8 and 9 report the results of the second experimental test. In this test, the chaser spacecraft, which starts from an offset position and attitude, first zeros out the transversal and angular errors and then follows a straight longitudinal reference line toward the target, to which eventually automatically docks as shown in Fig. 10. The entire maneuver lasts 189 s. The initial relative chaser position and attitude are

$${}^{\mathrm{tg}}x'_{\mathrm{ch}} = 0.34\ \mathrm{m}; \qquad {}^{\mathrm{tg}}z'_{\mathrm{ch}} = -1.5\ \mathrm{m}; \qquad \theta = -15.3\ \mathrm{deg} \tag{21}$$

As in the previous test, during the first 10 s the chaser vehicle is not floating and kept stationary while the Kalman filters converge. Then the vehicle is floated and the autonomous docking maneuver is conducted. The maneuver consists of the following four phases:

1) *Transversal error suppression (between time $A = 10$ s and $B = 30.4$ s)*: During this phase, as clearly shown in Fig. 8a, the lateral error is decreased via a bang-coast-bang motion. Meanwhile, as reported in Fig. 8c, the attitude is controlled to maintain the pointing toward the target by tracking the reference signal of Eq. (20).

2) *Coasting toward the target (between time B and $C = 72.8$ s)*: During this phase the relative longitudinal distance is reduced via a nominal bang-coast-bang motion as shown in Fig. 8b, while the transversal displacement and relative attitude are kept about zero as reported in Figs. 8a and 8c.

3) *Way point navigation to the target in preparation of the soft docking (between time C and $D = 167.8$ s)*: This phase begins when a relative longitudinal distance of 0.6 m is reached. The vehicle is basically stopped at this point. Then, by using the stair-shape reference curve shown in Fig. 8b, the chaser vehicle approaches the target through a set of way points with a glide path speed profile. At time D, just before the engaging phase, the transversal error is 0.018 m, the longitudinal error is -0.015 m, and the attitude error is -0.6 deg (with the zeros corresponding to the nominal values for docking). These values are well within the docking tolerances

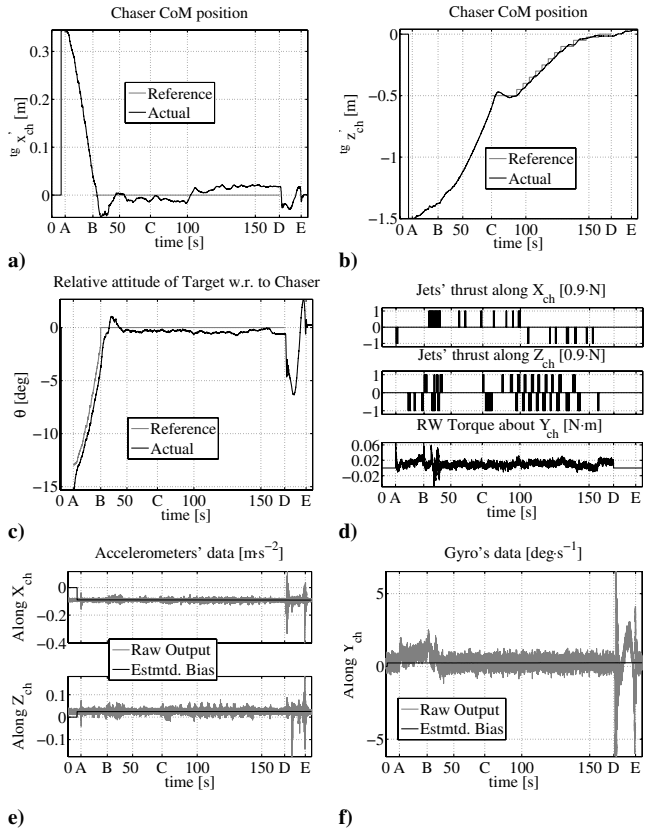

Fig. 8 Results of experimental test 2, autonomous approach and docking to the target: logged data versus time. The chaser spacecraft simulator starts to float at time $A = 10$ s. The docking mechanism starts to engage at time $D = 167.8$ s. At time $E = 183.8$ s the chaser vehicle is completely docked to the target. a) Transversal position of the center of mass of the chaser with respect to the target; b) longitudinal position of the center of mass of the chaser; c) relative attitude; d) actuators' actions; e) accelerometers' data; and f) gyroscope's data.

reported in Table 1. Furthermore, the relative transversal, longitudinal, and attitude speed components are basically zero as evidenced by the flatness of the curves in Figs. 8a–8c during the time instants before D.

4) *Soft docking by engaging of the Starsys docking interface (between time D and $E = 183.8$ s)*: As the mechanism starts to engage, at time D, the vehicle control is shut off, as shown in Fig. 8d, and any subsequent relative motion, between times D and E, is due to the action of the docking mechanism. Finally, at time E the chaser is completely docked to the target as shown in Fig. 10. The oscillations occurring about time E, shown, in particular, in Fig. 8e, are due to the dynamics of the springs embedded in the docking interface.

The tracking errors during this maneuver are as follows. The mean of the absolute value of the relative attitude error $\Delta(\theta)$, between times A and D, is 0.57 deg with standard deviation of 0.5 deg. The mean of the absolute value of $\Delta({}^{tg}x'_{ch})$, between times B and D, is 0.015 m with standard deviation of 0.008 m. Finally, the mean of the absolute value of $\Delta({}^{tg}z'_{ch})$, between times C and D, is 0.017 m with standard deviation of 0.01 m.

Figures 8e and 8f show that also in this test the navigation Kalman filters correctly estimate the biases of the accelerometers and gyroscopes. Figure 9 shows a bird's-eye view of the motion of the chaser spacecraft simulator during the docking maneuver.

The equivalent volume of propellant air consumed during this experimental test was ~ 0.12 m^3 (at the reference pressure of 0.35 MPa).

V. Conclusion

A new planar laboratory test bed was introduced for the simulation of the autonomous approach and docking of a chaser spacecraft to a target spacecraft of similar mass. The test bed consists of chaser and target vehicle simulators floating via air pads on a flat floor. The simulators integrate the docking interface mechanism prototype for DARPA's Orbital Express mission. Vision and inertial data fusion is used for the relative navigation of the chaser simulator; linear PD attitude control is used to command its reaction wheel, and a nonlinear translation control approach based on Schmitt triggers is used to command its thrusters.

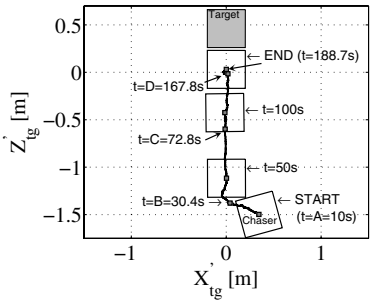

Fig. 9 Results of experimental test 2, autonomous approach and docking to the target: bird's-eye view of the motion of the chaser spacecraft simulator on the epoxy floor. The line indicates the ground track of the chaser center of mass. The empty squares are snapshot sketches of the chaser vehicle at significant time instants during the maneuver. At the end of the maneuver the chaser is docked to the target as shown in Fig. 10.

The presented experimental tests of autonomous proximity maneuver of the spacecraft chaser simulator and autonomous docking to the target simulator are significant sample cases of the capability of the new test bed. In particular, the experimental results, which showed a good repeatability and robustness against disturbance, validated the proposed estimation and control approaches. The achieved accuracy in following the reference trajectory (respectively, ~ 1 cm for the translation and ~ 0.1 deg for the rotation) and docking to the target with a very low relative velocity (<1 mm s^{-1}) is considerably higher than the one strictly needed by the docking interface.

Although the flotation of spacecraft simulators over a flat floor, exploited in our test bed, allows experiments to be conducted only in two dimensions, it provides a better level of gravity reduction than parabolic flights and offers a low-risk and relatively low-cost intermediate validation step between analytical–numerical simulations and flight missions for proximity navigation and docking operations. Furthermore, the algorithms proposed in the paper for the

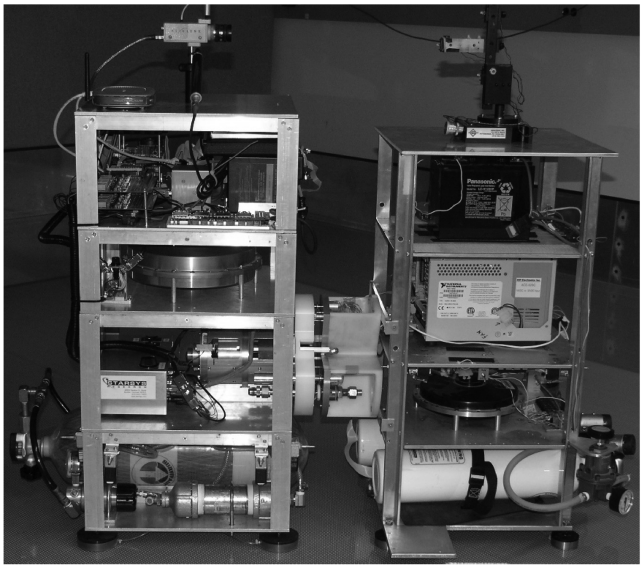

Fig. 10 The chaser spacecraft simulator (on the left-hand side) docked to the target spacecraft simulator (on the right-hand side) at the end of the experimental test 2.

vision sensor, the estimation, and the control can be in principle extended to three-dimensional applications.

The three main simplifying hypotheses made in our research were to consider the target spacecraft attitude stabilized, to consider the proximity navigation and docking maneuvers fast with respect to the orbital period, and to have the chaser vehicle fixed during initialization of the navigation Kalman filters. These assumptions will be dropped during follow-on research.

Acknowledgment

This research was sponsored by the U.S. Air Force Research Laboratory—Space Vehicles Directorate.

References

[1] Polites, M. E., "An Assessment of the Technology of Automated Rendezvous and Capture in Space," NASA TP-1998-208528, 1998.

[2] Kawano, I., Mokuno, M., Kasai, T., and Suzuki, T., "Result of Autonomous Rendezvous and Docking Experiment of Engineering Test Satellite-VII," *Journal of Spacecraft and Rockets*, Vol. 38, No. 1, 2001, pp. 105–111.

[3] Fehse, W., *Automated Rendezvous and Docking of Spacecraft*, Cambridge Univ. Press, Cambridge, U.K., 2003.

[4] Choset, H., and Kortenkamp, D., "Path Planning and Control for AERCam a Free-Flying Inspection Robot in Space," *Journal of Aerospace Engineering*, Vol. 12, No. 2, 1999, pp. 74–81.

[5] Underwood, C. I., Richardson, G., and Savignol, J., "In-Orbit Results from the SNAP-1 Nano-Satellite and Its Future Potential," *Philosophical Transactions of the Royal Society of London, Series A: Mathematical and Physical Sciences*, Vol. 361, Dec. 2003, pp. 199–203.

[6] Davis, T. M., and Melanson, D., "XSS-10 Micro-Satellite Flight Demonstration Program Results," *Proceedings of SPIE Conference on Spacecraft Platforms and Infrastructure*, SPIE–International Society for Optical Engineering, Bellingham, WA, 2004, Vol. 5419, pp. 16–25.

[7] Ruth, M., and Tracy, C., "Video-Guidance Design for the DART Rendezvous Mission," *Proceedings of SPIE Conference on Spacecraft Platforms and Infrastructure*, SPIE–International Society for Optical Engineering, Bellingham, WA, 2004, Vol. 5419, pp. 92–106.

[8] Shoemaker, J., and Wright, M., "Orbital Express On-Orbit Satellite Servicing Demonstration," *Proceedings of SPIE Conference on Spacecraft Platforms and Infrastructure*, SPIE–International Society for Optical Engineering, Bellingham, WA, 2004, Vol. 5419, pp. 57–65.

[9] Carignan, C. R., and Akin, D. L., "The Reaction Stabilization of On-Orbit Robots," *Control Systems Magazine, IEEE* , Vol. 20, No. 6, Dec. 2000, pp. 19–33.

[10] Creamer, G., Pipitone, F., Gilbreath, C., Bird, D., and Hollander, S., "NRL Technologies for Autonomous Spacecraft Rendezvous and Proximity Operations," AAS 03-272, 2003.

[11] Colmenarejo, P., Gandia, F., Barrena, V., and Tomassini, A., "Platform: A Test-Bench to Test GNC Algorithms and Sensors for Formation Flying, RvD and Robotic Applications," *Proceedings of the 4th International Workshop on Satellite Constellations and Formation Flying*, National Institute for Space Research, São José dos Campos, Brazil, 2005.

[12] Schwartz, J., Peck, M., and, Hall C. D., "Historical Review of Spacecraft Simulators," *Journal of Guidance, Control, and Dynamics*, Vol. 26, No. 4, 2003, pp. 513–522.

[13] Machida, K., Toda, Y., and Toshiaki, I., "Maneuvering and Manipulation of Flying Space Telerobotics System," *Proceedings of IEEE International Conference on Intelligent Robots and Systems*, IEEE, Piscataway, NJ, 1992, pp. 3–10.

[14] Ullman, M. A., Experiments in Autonomous Navigation and Control of a Multi-Manipulator Free Flying Space Robots, Ph.D. Thesis, Stanford University, Stanford, CA, 1993.

[15] Corazzini, T., and How, J. P., "Onboard GPS Signal Augmentation for Spacecraft Formation Flying," *Proceedings of the Institute of Navigation GPS-98 Conference*, The Institute of Navigation, Fairfax, VA, 1998, pp. 1937–1946.

[16] Marchesi, M., Angrilli, F., and Venezia, R., "Coordinated Control for Free-Flyer Space Robots," *IEEE International Conference on Systems, Man, and Cybernetics*, IEEE, Piscataway, NJ, 2000, Vol. 5, pp. 3550–3555.

[17] Ledebuhr, A. G., Ng, L. C., Jones, M. S., Wilson, B. A., Gaughan, R. J., Breitfeller, E. F., Taylor, W. G., Robinson, J. A., Antelman, D. R., and Nielsen, D. P., "Micro-Satellite Ground Test Vehicle for Proximity and Docking Operations Development," *Proceedings of IEEE Aerospace Conference*, IEEE, Piscataway, NJ, 2001, Vol. 5, pp. 2493–2504.

[18] Nolet, S., Kong, E., and Miller, D. W., "Design of an Algorithm for Autonomous Docking with a Freely Tumbling Target," *Proceedings of SPIE Modeling, Simulation, and Verification of Space-Based Systems*, SPIE–International Society for Optical Engineering, Bellingham, WA, 2005, pp. 123–134.

[19] Shay, T. J., "Design and Fabrication of a Planar Autonomous Docking Simulator with Fluid Transfer Capability," M.S. Thesis, Naval Postgraduate School, Monterey, CA, 2005.

[20] Friedman, D. A., "Laboratory Experimentation of Autonomous Spacecraft Docking using Cooperative Vision Navigation," M.S. Thesis, Naval Postgraduate School, Monterey, CA, 2005.

[21] Yaniec, J. S., and Del Rosso, C., "Experiment Design Requirements and Guidelines," NASA 932 C-9B-AOD 33897, 2005.

[22] Stamm, S., and Motaghedi, P., "Orbital Express Capture System: Concept to Reality," *Proceedings of SPIE Conference on Spacecraft Platforms and Infrastructure*, SPIE–International Society for Optical Engineering, Bellingham, WA, 2004, Vol. 5419, pp. 78–91.

[23] Dobrokhodov, V., and Lizarraga, M., "Developing Serial Communication Interfaces for Rapid Prototyping of Navigation and Control Tasks," AIAA 2005-6099, 2005.

[24] Romano, M., "On-the-Ground Experiments of Autonomous Spacecraft Proximity Navigation Using Computer Vision and Jet Actuators," *Proceedings of IEEE International Conference on Advanced Intelligent Mechatronics*, SPIE–International Society for Optical Engineering, Bellingham, WA, 2005, pp. 1011–1016.

[25] Gelb, A. (ed.), *Applied Optimal Estimation*, MIT Press, Cambridge, MA, 1974.

[26] Crassidis, J. L., and Junkins, J. L., *Optimal Estimation of Dynamic Systems*, Chapman & Hall/CRC, Boca Raton, FL, 2004.

[27] Bryson, A. E., *Control of Spacecraft and Aircraft*, Princeton Univ. Press, Princeton, NJ, 1993.

[28] Wie, B., *Space Vehicle Dynamics and Control*, AIAA Education Series, AIAA, Reston, VA, 1998.

C. McLaughlin
Associate Editor